catalysts

MDPI

Article

Hydrogen Production from Ethanol Steam Reforming by Stable $LaNi_xCu_{1-x}O_{3-\lambda}$ Perovskite-Type Catalysts

Chenjie Ruan, Binlin Dou *, Na Chen and Hua Zhang

School of Energy and Power Engineering, University of Shanghai for Science and Technology, Shanghai 200093, China; ruanchenjie2024@163.com (C.R.); chenna199805@163.com (N.C.); zhanghua3000@163.com (H.Z.)
* Correspondence: bldou@usst.edu.cn; Tel.: +86-2155271456

Abstract: Hydrogen production from ethanol steam reforming (ESR) was performed using the synthesized $LaNi_xCu_{1-x}O_{3-\lambda}$ perovskite-type catalysts in a continuous two-stage fixed-bed reactor from 450 to 700 °C under atmospheric pressure. The elemental analysis (EA), XRD, SEM, BET, and TGA-DTG technologies were used to characterize the structures and properties of the synthesized catalysts. The thermodynamic equilibrium model, based on the minimization of Gibbs free energy using a non-stoichiometric methodology, was carried out and compared with experimental data. The results demonstrated that the catalytic activity of the perovskite-type catalysts for ESR can be improved after modification with a certain amount of copper (about 0.67 mmol/g) and decreased further with an increase in copper content (about 3.41 mmol/g). The most active catalyst was found to be $LaNi_{0.9}Cu_{0.1}O_{3-\lambda}$, with an ethanol conversion value of 96.0% and hydrogen selectivity of 71.3%. The perovskite-type catalysts with an appropriate amount of Cu promoter improved coking resistance and presented excellent stability with no loss of activity over 101 h at 700 °C. Based on the power-law kinetic model with the first reaction order, the activation energy and the frequency factor for ethanol steam reforming by perovskite-type catalysts were calculated. Our studies indicated the enhanced effects of Ni and Cu on the small Ni-Cu bimetallic particles in the water gas shift (WGS) reaction, which could also contribute to the activity and stability of the $LaNi_xCu_{1-x}O_{3-\lambda}$ perovskite-type catalysts in hydrogen production.

Keywords: ethanol steam reforming (ESR); copper promoted $LaNi_xCu_{1-x}O_{3-\lambda}$ perovskite-type catalysts; hydrogen production

check for updates

Academic Editors: Thien An Le, Charles Xu and Huyen Tran Dang

Received: 12 December 2024
Revised: 23 December 2024
Accepted: 24 December 2024
Published: 26 December 2024

Citation: Ruan, C.; Dou, B.; Chen, N.; Zhang, H. Hydrogen Production from Ethanol Steam Reforming by Stable $LaNi_xCu_{1-x}O_{3-\lambda}$ Perovskite-Type Catalysts. *Catalysts* **2025**, *15*, 9. https://doi.org/10.3390/catal15010009

1. Introduction

Hydrogen production from the steam reforming of biomass-derived fuels is regarded as one of the promising ways to solve energy shortage and environmental pollution problems, and various technologies have been developed for its industrial application [1]. Compared with many oxygenated hydrocarbons from biomass, the ethanol produced economically and sustainably from forestry and agricultural waste has been considered as an attractive feedstock for hydrogen production due to its high H element content, nontoxicity, and easy transport [2]. An overall stoichiometric equation for ethanol steam reforming (ESR) is considered:

$$C_2H_5OH+3H_2O \overset{Ni}{\rightarrow} 2CO_2+6H_2, \Delta H > 0 \tag{R1}$$

The ESR process consists of many chemical reactions along with some parallel side reactions, and it also produces some undesired products such as CH_4, CO_2, CO, carbons, etc. [3]. Hydrogen production is mainly dependent on the properties of the catalysts and reaction conditions (time, temperature, etc.) [4,5]. The carbon deposition on the conventional catalysts is also inevitable, and the challenge is still to design and develop active and stable catalysts for hydrogen production from ESR [6,7]. Noble metal-based catalysts, including Au, Pd, Pt, Rh, Ru, etc., have presented excellent activity for ESR [8–11]. However, due to the high cost and the limited availability of noble metals, transient metal-based catalysts, such as Cu, Mn, Mo, Co, Fe, Ni, etc., have been studied and offer long-term performances in practical applications [12–16]. In the last few years, perovskites (ABO_3) have been used as catalysts and support materials for hydrogen production via catalytic steam reforming [17–19]. The results also demonstrated that high Ni dispersion on perovskite-type catalysts greatly promoted the breaking of C-H and C-C bonds, as well as dehydration and thermal decomposition, to produce hydrogen. Compared with traditional catalysts, this type of catalyst presented strong high coking resistance and long-term stability under steam reforming conditions [20,21]. Urasaki et al. performed ESR via $SrTiO_3$, $LaAlO_3$, and $BaTiO_3$ perovskite-type Ni and Co catalysts, and the results confirmed the improved activity and stability of perovskite-type catalysts [22]. In the perovskite structure, the A and B sites can be occupied by large cations with weaker interactions in A and small cations with stronger interactions in B, resulting in the modification of the properties of the catalysts.

Recently, the addition of the metals such as Fe, Mn, Mo, Co, and Cu as promoters has been studied to further improve the performances of catalysts for hydrogen production from steam reforming, and the advantage of these methods is their ability to overcome the activity and stability problems of conventional catalysts [23–25]. Wang et al. [23] studied Ni-based catalysts through the addition of Fe for the steam reforming of biomass-derived liquid feedstock, and the results indicated the formation of Fe-Ni, with the Fe particles on the Ni surface of the catalyst to increase the activity and selectivity of the catalyst, as well as to inhibit carbon formation and deposition. Heo et al. [24] studied the addition of Mn on reforming catalysts to improve the activity and stability in ESR due to the synergistic effects of Mn and Ni atoms. Nejat et al. [25] studied ESR via the bimetallic Ni-Co catalysts, and the results demonstrated that the catalysts of complex metals have better catalytic activity than mono-metallic catalysts. However, the Ni-Co catalysts seemed to present poor stability; the Ni and Co surface layers were gradually oxidized as the reaction progressed, thus causing the deactivation of the catalyst [26]. Yu et al. [27] studied Cu-doped Ni-Mg-Al catalysts for ESR, and the results found that the addition of a tiny amount of copper increased the reducibility and activity of catalysts; however, the hydrogen selectivity was still very low. As reported in the literature [28], a small amount of copper promoted as an active agent was very beneficial to dehydrogenation and WGS reaction, while more Ni active particles were beneficial to C-C bond breakage during the ESR process to increase H_2 selectivity. Lowering the activation energy of ESR is made possible through the use of a copper-promoted perovskite-type catalyst to increase the conversion of the feeding and selectivity of hydrogen.

To date, the utilization of the copper-promoted perovskite-type catalysts for the ESR process is not common. In this paper, the new Ni-based perovskite-type catalysts with a Cu promoter were synthesized via the co-precipitation method to generate high stability and high activity, and hydrogen production from ESR was performed in a continuous two-stage fixed-bed reactor from 450 °C to 700 °C. The influence of Cu content on the catalytic activity and long-term stability of the catalysts during ESR were experimentally evaluated.

2. Results and Discussion

2.1. Characterization of Catalysts

The properties of the fresh synthesized perovskite-type $LaNi_xCu_{1-x}O_{3-\lambda}$ catalysts are shown in Table 1. The BET specific surface area of perovskite-type catalysts was low, which might be due to the high temperature conditions for the synthesis of perovskite oxides [29,30]. The TGA-DTG curves of the $LaNi_xCu_{1-x}O_{3-\lambda}$ precursor before the calcination are shown in Figure 1. The thermogravimetric curves mainly included four stages of mass loss from room temperature to 900 °C: the first stage occurred before the temperature of 110 °C, which is mainly caused by the evaporation of water adsorbed on the precursor, including the washing process. The second stage started from 150 °C and continued to 220 °C, which was mainly caused by the crystallization of water in the precursor. The third stage occurred in the range of 300–500 °C, which was caused by the decomposition of $La(OH)_3$, $Cu(OH)_2$, and $Ni(OH)_2$ to form corresponding oxides. The last stage occurred at 700–780 °C, which was attributed to the transformation process of the decomposition of some residual precursors into metal oxides and the metal oxides produced by decomposition to form perovskite; the mass no longer decreased after 780 °C, indicating a stable crystalline structure, as shown in Figure 2.

Table 1. The properties of fresh catalysts.

Catalysts	S_{BET} (m^2/g)	V_{pore} (cm^3/g)	Content (mmol/g)		Average Pore Size (nm)
			Ni	Cu	
$LaNiO_{3-\lambda}$	4.52	0.253	6.83	-	46.5
$LaNi_{0.5}Cu_{0.5}O_{3-\lambda}$	5.51	0.257	3.41	3.41	45.3
$LaNi_{0.9}Cu_{0.1}O_{3-\lambda}$	6.73	0.266	6.16	0.67	43.6

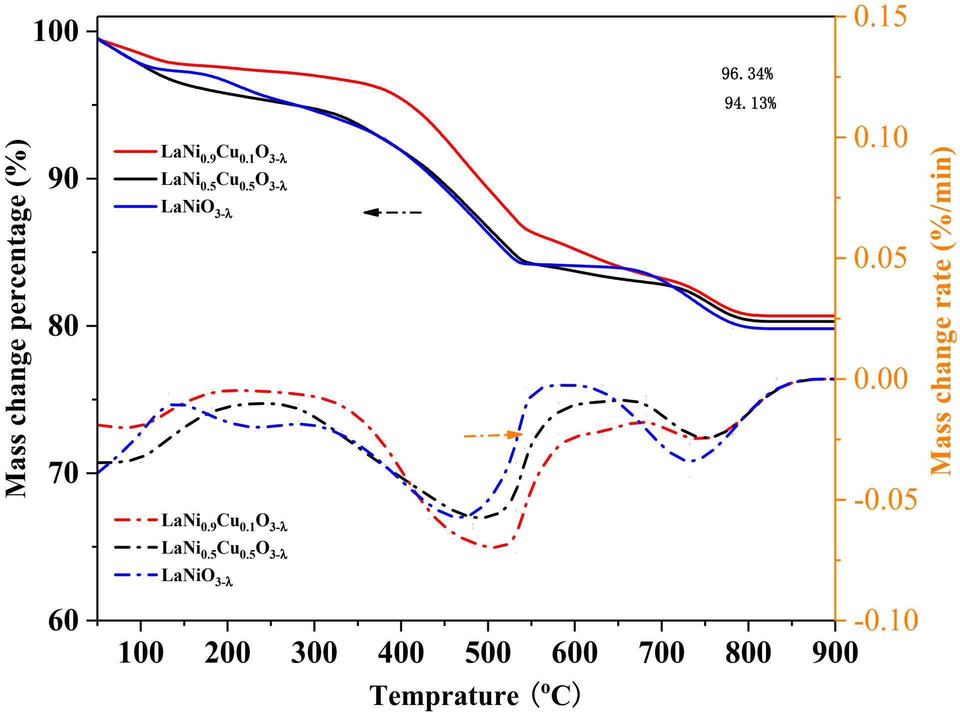

Figure 1. TGA-DTG curves of the catalysts precursor before the calcination.

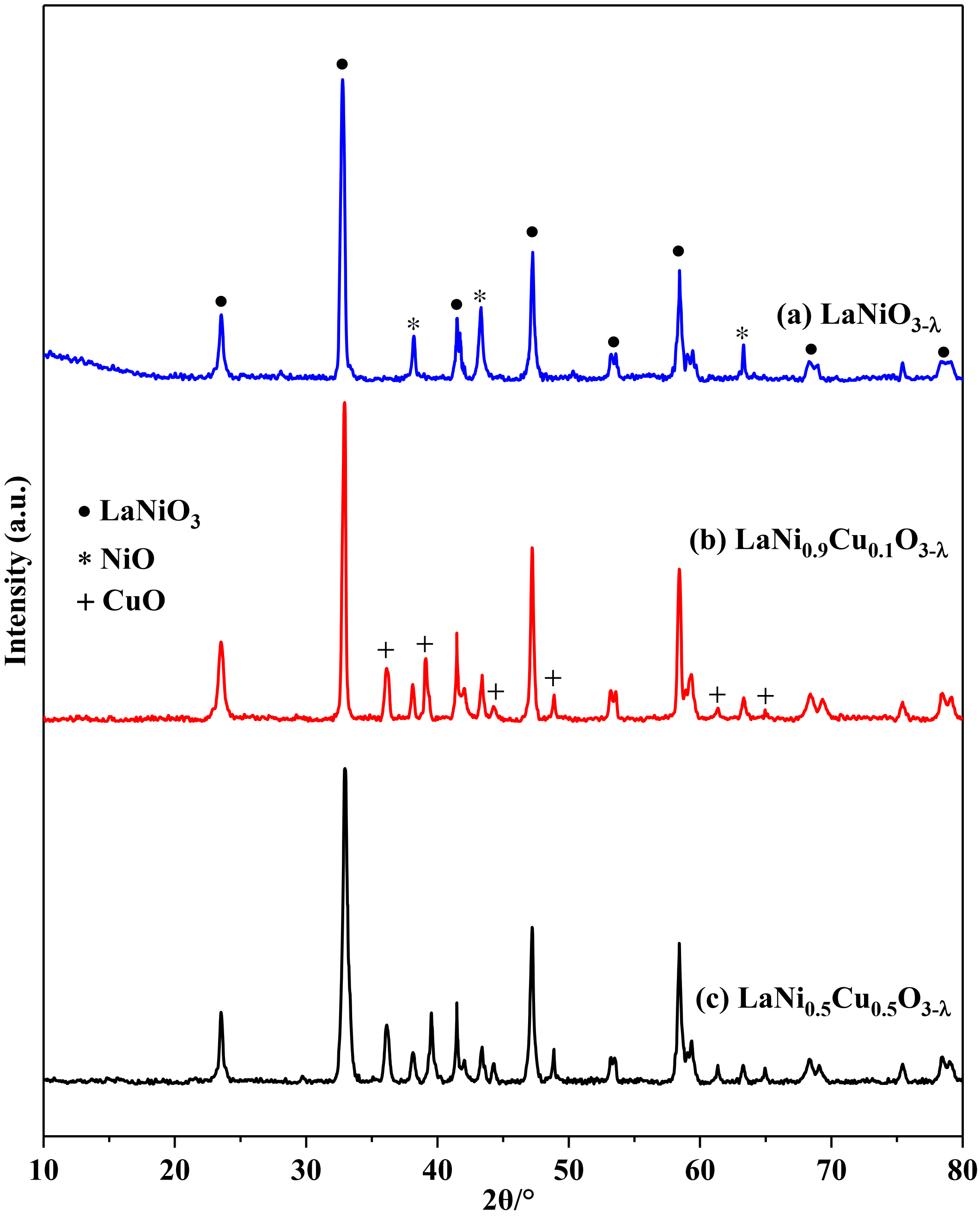

Figure 2. XRD patterns of fresh catalysts.

The XRD patterns of the $LaNi_xCu_{1-x}O_{3-\lambda}$ catalysts are shown in Figure 2. The diffraction peaks at 2θ = 38.2, 43.3, and 63.3° were assigned to NiO, and the diffraction peaks at 2θ = 23.5, 32.8, 41.5, 47.2, 53.2, 58.4, 68.3, and 78.4° were assigned to perovskite-type catalysts with the hexagonal phase structures (ABO_3). Nevertheless, the incorporation of Cu on perovskite catalysts indicated that the additional CuO peaks observed at 2θ = 36.1, 39.1, 44.3, 48.9, 61.4, and 65.0° did not change the perovskite-type phase structures. The intensity of the CuO peaks increased with the contents of copper, increasing from 0.1 to 0.5, and with the introduction of the Cu element, the (110) crystal diffraction peaks remained single and were not divided into the multiple-peaks. The positions of the peaks were also not shifted. The results show that the perovskite structure of the Cu-modified catalyst remains unchanged, which is beneficial for the activity and stability of the catalyst.

As shown in Figure 3, the reducibility of $LaNi_xCu_{1-x}O_{3-\lambda}$ catalysts was also investigated using H_2-TPR. Three peaks of hydrogen consumption were observed in all catalysts. Generally, there were consumption peaks of H_2 in the case of perovskites because of the reduction in the B site metal cation in the ABO_3 structure. The first minor peak at 300 °C was due to the reduction in Ni^{2+} in the perovskite structure to an intermediate-valence Ni cation, leading to the formation of $La_4Ni_3O_{10-\lambda}$ [31]. The intense peak with the temperature at 470 °C was attributed to the reduction of $La_4Ni_3O_{10}$ to Ni^{2+}, which leads to the formation of $La_2NiO_{4-\lambda}$. The third peak at 598, 638, and 656 °C might be due to the complete reduction in Ni^{2+} in $La_2NiO_{4-\lambda}$ to produce La_2O_3, Cu, and Ni metallic nanoparticles [32,33], which was due to the following:

$$4LaNiCuO_{3-\lambda} + 2H_2 \rightarrow La_4Ni_3O_{10-\lambda} + Ni + 2H_2O \quad \text{(R2)}$$

$$La_4Ni_3O_{10-\lambda} + 3H_2 \rightarrow La_2NiO_{4-\lambda} + 2Ni + La_2O_3 + 3H_2O \quad \text{(R3)}$$

$$La_2NiO_{4-\lambda} + H_2 \rightarrow Ni + La_2O_3 + H_2O \quad \text{(R4)}$$

$$2\ LaNi_xCu_{1-x}O_{3-\lambda} + 3H_2 \rightarrow 2Ni + La_2O_3 + 2Cu + 3H_2O \quad \text{(R5)}$$

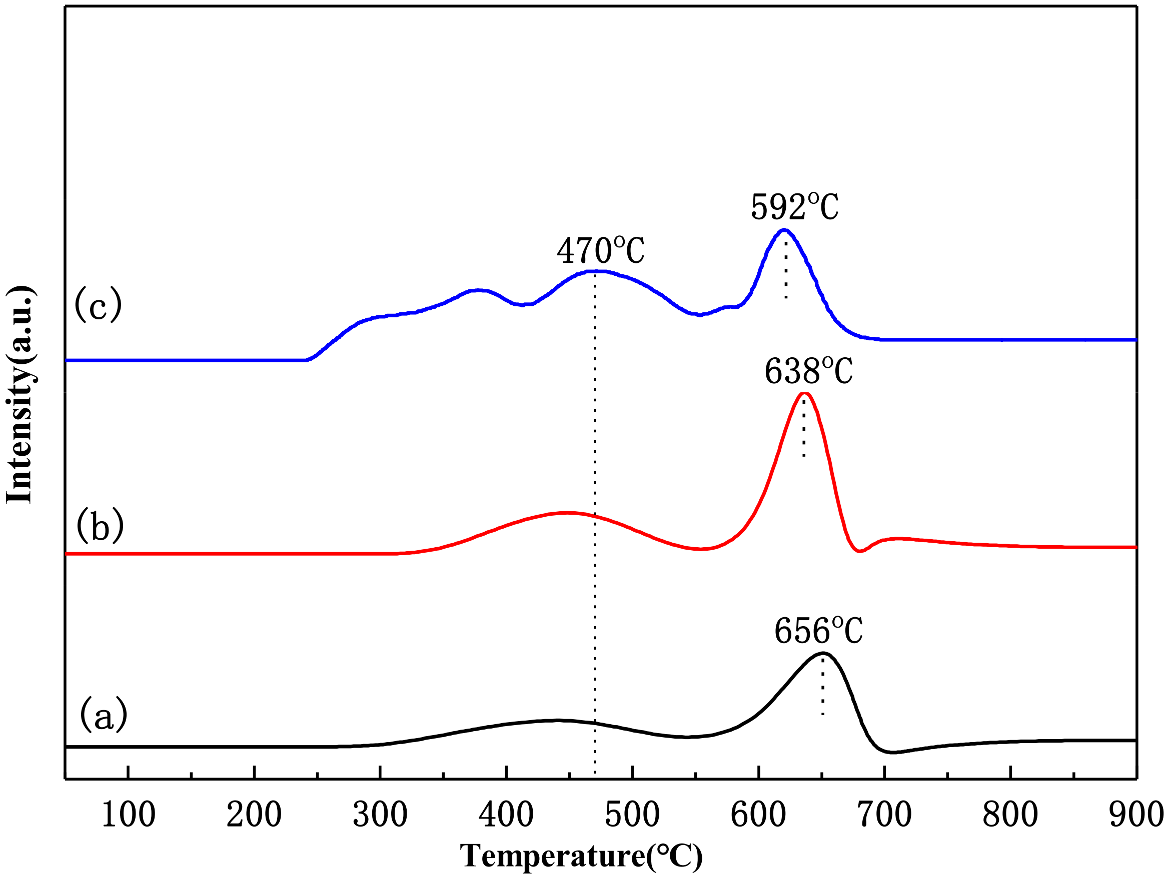

Figure 3. TPR profiles of catalysts: (**a**) $LaNiO_{3-\lambda}$; (**b**) $LaNi_{0.9}Cu_{0.1}O_{3-\lambda}$; (**c**) $LaNi_{0.5}Cu_{0.5}O_{3-\lambda}$.

The area of the second reduction peak was greater than the first one, which might be due to the fact that the amount of Ni^{2+} reduced in the second stage contains the Ni^{2+} reduced in the first stage [34]. Furthermore, the superior peaks shifted towards lower temperature and presented stronger intensity with the addition of Cu, indicating that the synergistic effect of Cu and Ni on the increased reducibility causes the high-valent ions to be more easily reduced. The amounts of H_2 consumption calculated from the peaks were decreased as $LaNi_{0.9}Cu_{0.1}O_{3-\lambda}$ > $LaNi_{0.5}Cu_{0.5}O_{3-\lambda}$ > $LaNiO_{3-\lambda}$, and most Ni species in the three catalysts could be reduced to metal sites.

The scanning electron microscope (SEM) images of $LaNi_xCu_{1-x}O_{3-\lambda}$ catalysts are shown in Figure 4a–c. It can be seen from Figure 4a that the particle size of the sample with $x = 1.0$ was smaller and showed an irregular small block structure when the copper was not doped. The $LaNi_{0.9}Cu_{0.1}O_{3-\lambda}$ showed a regular spherical shape structure with some agglomeration. When the doping amount of copper was up to 0.5, the particle sizes of the catalyst became larger, showing a patchy structure. According to the kinetics of grain growth, the growth of grain morphology varies with the growth rate of the crystal plane. The overall morphology of catalysts would be affected by the copper doping, and the perovskite exhibited a larger bulk structure and had a smaller specific surface area with a high amount of Cu-doping, which was not conducive to the subsequent stage of ESR. To investigate the distribution of Cu, Ni, and La in the $LaNi_{0.9}Cu_{0.1}O_{3-\lambda}$ catalysts, the EDS-mapping method was used. As expected, the Cu, Ni, and La were distributed very evenly, and the Cu particles were highly dispersed on the Ni nanoparticles (Figure 5).

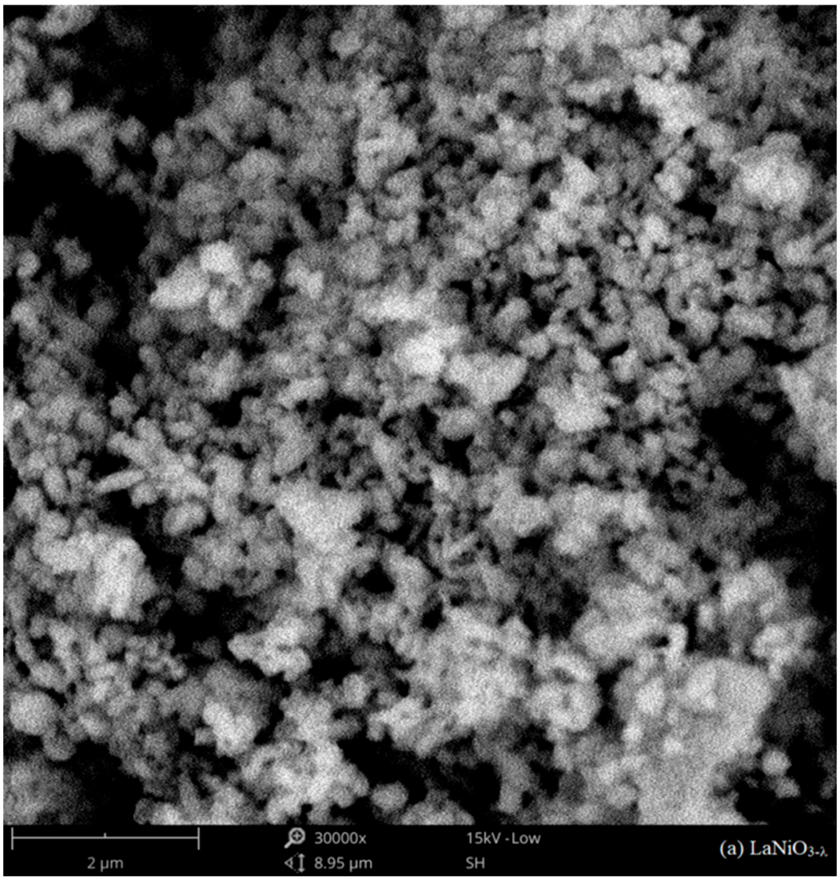

Figure 4. *Cont.*

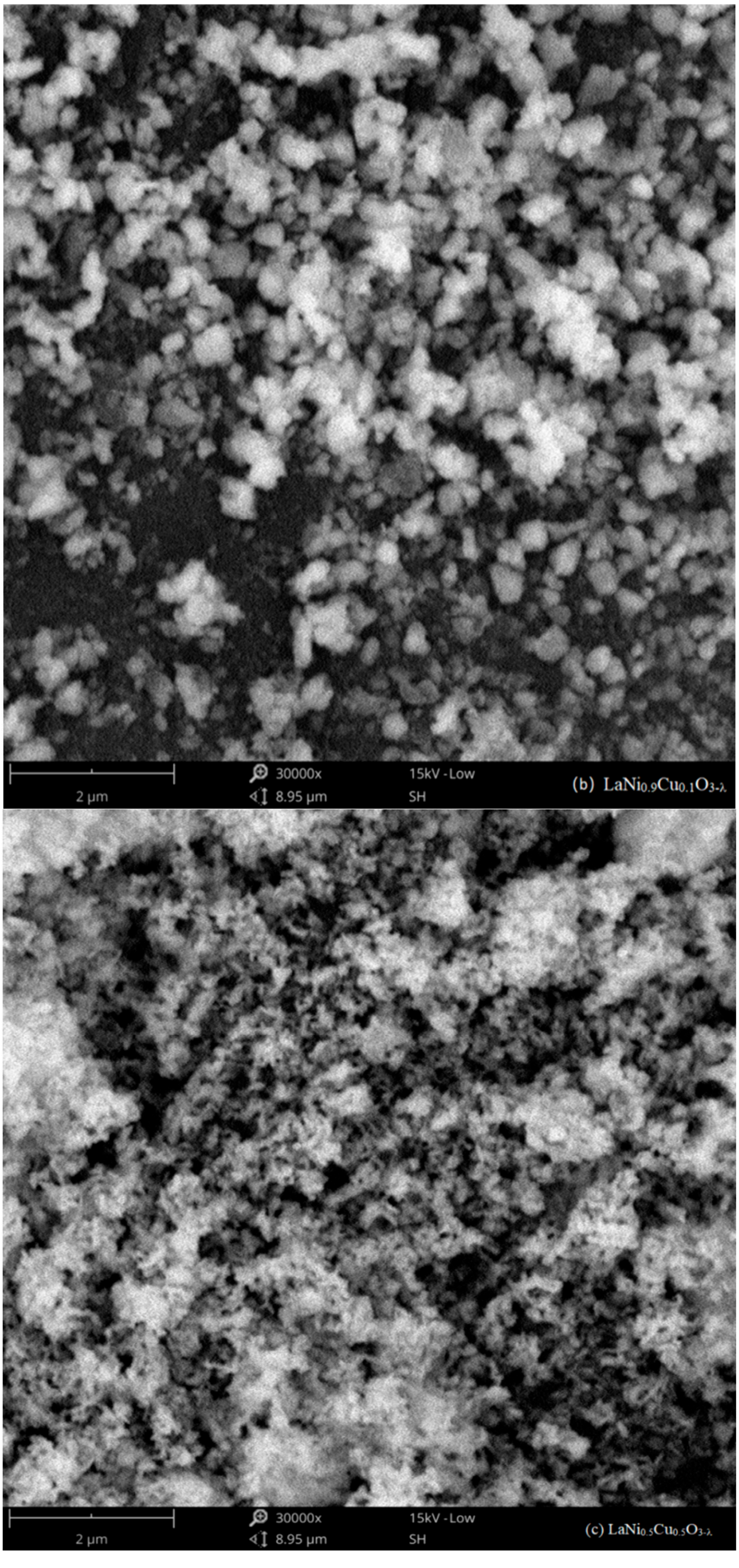

Figure 4. SEM of fresh catalysts: (**a**) $LaNiO_{3-\lambda}$; (**b**) $LaNi_{0.9}Cu_{0.1}O_{3-\lambda}$; (**c**) $LaNi_{0.5}Cu_{0.5}O_{3-\lambda}$.

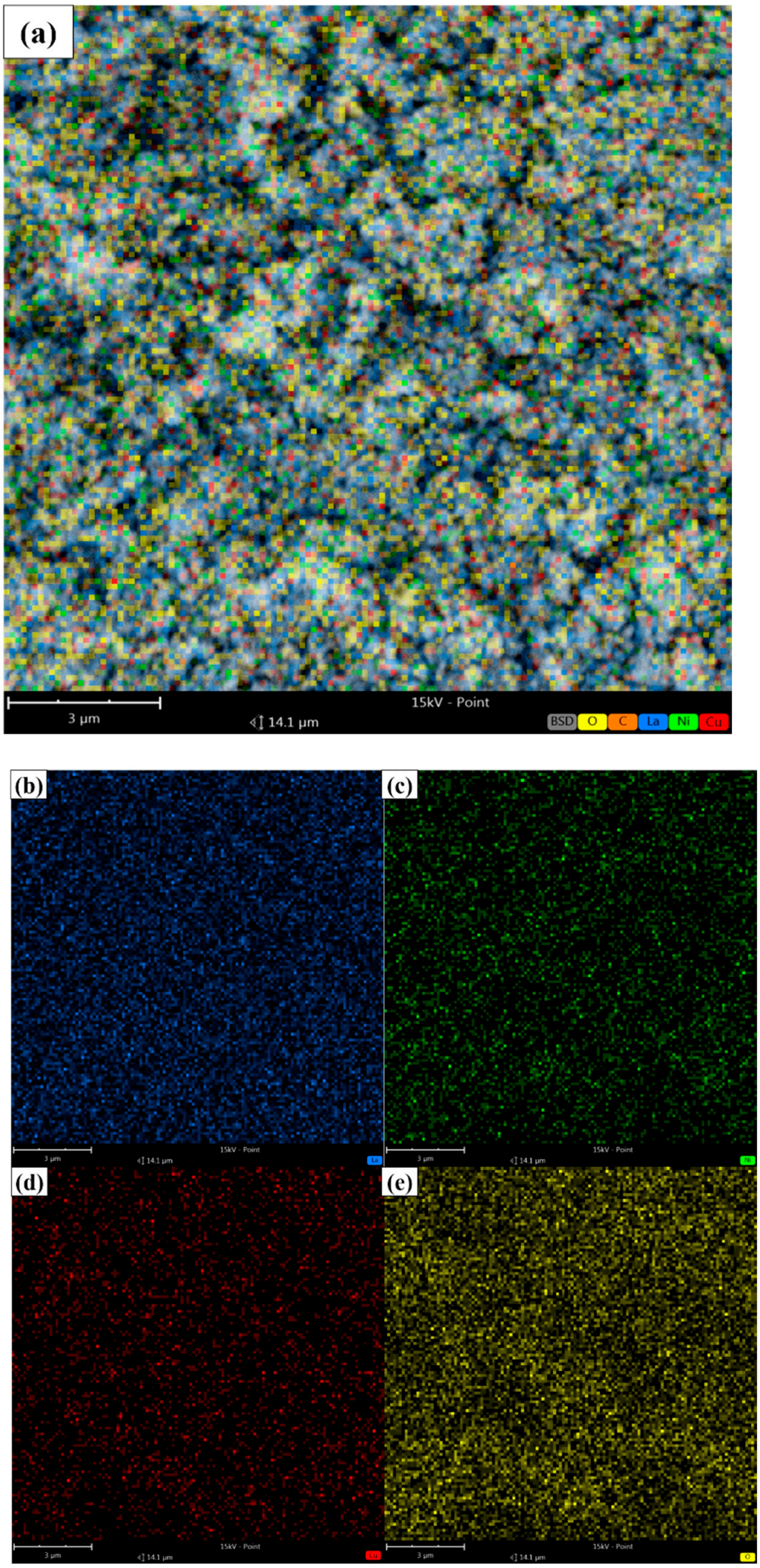

Figure 5. Total elementals mapping images of $LaNi_{0.9}Cu_{0.1}O_{3-\lambda}$ (**a**) and individual element mapping images: (**b**) La; (**c**) Ni; (**d**) Cu; and (**e**) O.

2.2. Hydrogen Production from ESR

The ethanol steam reforming proceeds via the following equations:

$$\text{Steam reforming}: \ C_2H_5OH \overset{H_2O}{\rightarrow} 2CO + 4H_2 \tag{R6}$$

$$\text{WGS}: \ CO + H_2O \leftrightarrow CO_2 + H_2 \tag{R7}$$

Possible side reactions involve CO methanation and carbon formation:

$$CO + 3H_2 \leftrightarrow CH_4 + H_2 \tag{R8}$$

$$CH_4 \rightarrow C + 2H_2 \tag{R9}$$

In this process, steam reforming of methane can also be catalyzed to produce H_2 via the following reactions:

$$CH_4 + 2H_2O \leftrightarrow CO_2 + 4H_2 \tag{R10}$$

$$CH_4 + H_2O \leftrightarrow CO + 3H_2 \tag{R11}$$

The carbon formation is inevitable; however, it need not be calculated in thermodynamic analysis because the Gibbs free energy is independent of carbon (the free energy of the solid formation is zero). The system under the conditions of high temperature and low pressure was also considered as ideal. The possible gases in the system were defined as CO, CH_4, H_2, CO_2, C_2H_5OH, and H_2O. The non-linear equations in the thermodynamic analysis were solved using an in-house Fortran Code based on the DNEQNF subroutine of the IMSL library. The initial molar number of ethanol was taken as 1 mole; the molar numbers of H_2O and products depended on the ratio of water to carbon (S/C) and nitrogen feed.

Figure 6 shows the thermodynamic equilibrium and experimental data on ethanol steam reforming under the conditions of S/C = 3:1 and a temperature from 450 to 700 °C. The system with high temperature and low pressure was also considered as ideal. The carbon formation is inevitable; however, it was not calculated in thermodynamic analysis since the free energy of carbon formation is zero. The conversions of ethanol and steam and the numbers of moles of H_2, CO_2, and CO increase with the increase in temperatures, and the number of moles of CH_4 decreases. The experimental ethanol conversions by $LaNi_xCu_{1-x}O_{3-\lambda}$ catalyst are 68.5–96.0% at 450–700 °C compared with 82.2–98.5% from the predicted equilibrium conversions. Concerning steam conversion, the values of 16.5–20.3%, found experimentally at 450–700 °C, are also small compared with the calculated equilibrium values of 20.0–22.1%. The thermodynamics results also show that feeding conversion and hydrogen production can reach acceptable values at low temperatures; however, high temperatures for ESR with catalysts seem to be necessary to maximize carbon suppression.

The hydrogen concentration predicted from thermodynamic equilibrium increases with the increasing temperature, and the ratios of H_2 moles to ethanol are 3.3, 3.5, 4.0, 4.4, 4.8, and 5.1 at 450 °C, 500 °C, 550 °C, 650 °C, and 700 °C, respectively. With high selectivity by the $LaNi_xCu_{1-x}O_{3-\lambda}$ catalyst, the composition of the gaseous products was very similar to the thermodynamic equilibrium. The concentrations of CO and CO_2 increase with the increasing temperature from 450 °C to 700 °C. This should be very important for $LaNi_xCu_{1-x}O_{3-\lambda}$ catalysts in providing WGS activity and decreasing the selectivity of CO. The ethanol and steam conversion for the $LaNi_{0.9}Cu_{0.1}O_{3-\lambda}$ reached 96.0% and 20.3%, respectively. The ethanol and steam conversion for the $LaNi_{0.5}Cu_{0.5}O_{3-\lambda}$ was also up to 91.2% and 19.8%, respectively. The ethanol and steam conversion of the Cu-doped catalysts was higher than that of $LaNiO_3$ without the Cu component, which was only 88.3% and 19.7%, respectively.

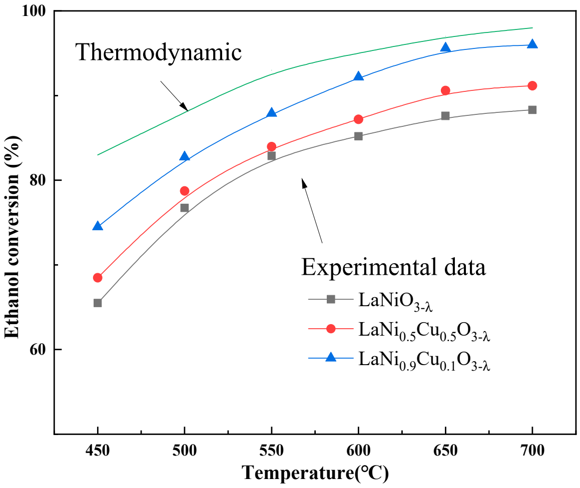

(**a**)

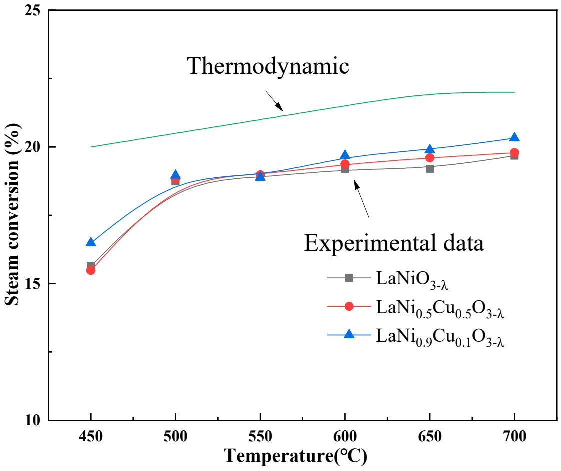

(**b**)

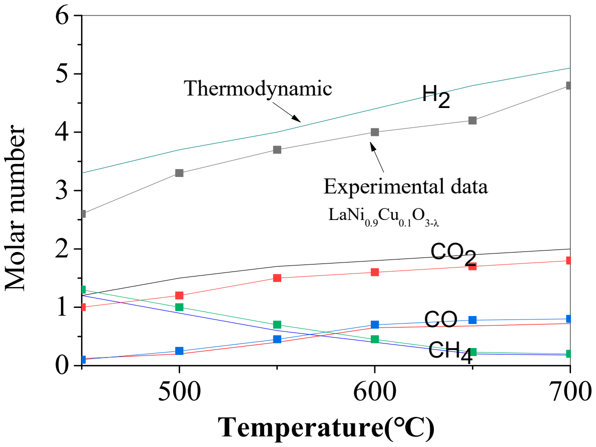

(**c**)

Figure 6. *Cont.*

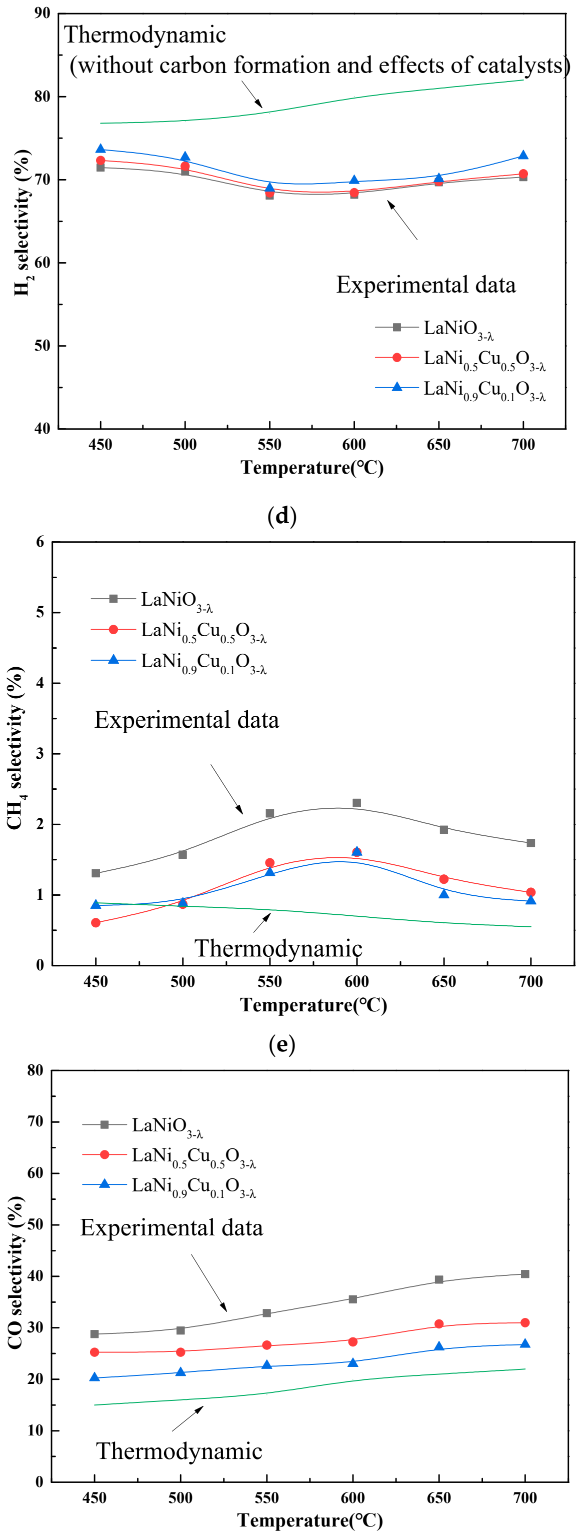

(**d**)

(**e**)

(**f**)

Figure 6. *Cont.*

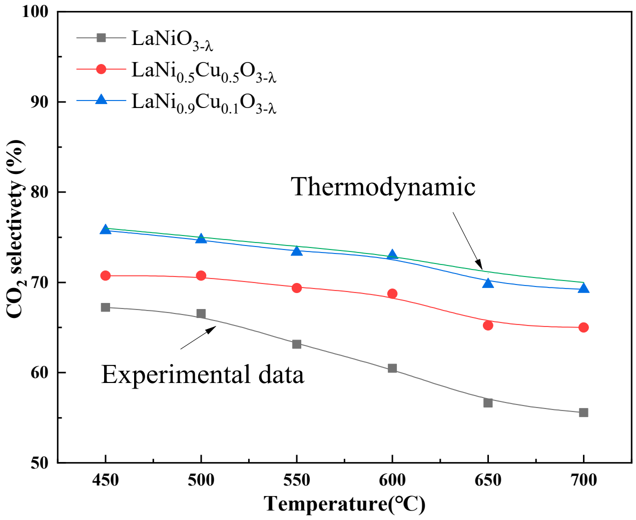

(**g**)

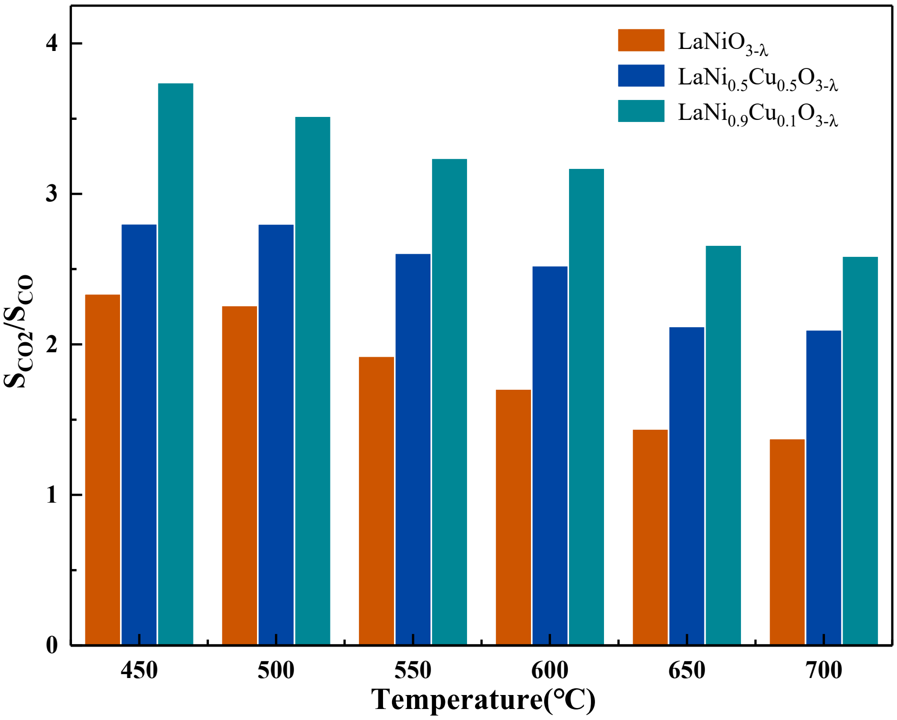

(**h**)

Figure 6. *Cont.*

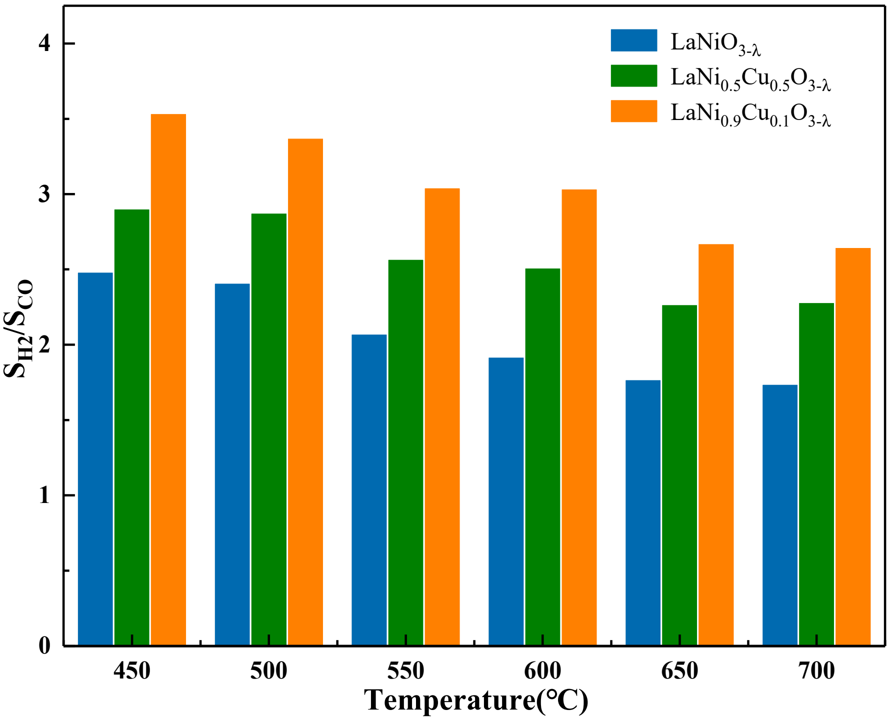

(**i**)

Figure 6. Thermodynamic equilibrium and experimental data on ethanol steam reforming: (**a**) ethanol conversion; (**b**) steam conversion; (**c**) number of moles; (**d**) H_2 selectivity; (**e**) CH_4 selectivity; (**f**) CO selectivity; (**g**) CO_2 selectivity; (**h**) S_{CO2}/S_{CO}; (**i**) S_{H2}/S_{CO}.

Methanation, WGS, and carbon formation were some of the major side reactions of ESR, which could have an impact on product distribution. As shown in Figure 6, the selectivity of CH_4 was very low for all catalysts, which revealed that methanation may be inhibited by $LaNi_xCu_{1-x}O_{3-\lambda}$ catalysts under the reaction conditions. Moreover, the addition of copper could facilitate the WGS reaction to increase H_2 selectivity. Similar studies have indicated the ratio of CO_2 to CO as a sign that the WGS reaction was related to the activity of the catalyst [35], and the results showed that the Cu-doped catalysts presented high H_2 and CO_2 selectivity and low CO selectivity, especially for $LaNi_{0.9}Cu_{0.1}O_{3-\lambda}$, which might be due to the very small amount of copper-facilitated ethanol dehydrogenation, the WGS reactions, and the enhanced distribution of active elements on the catalysts, with the effects of B-site doping on the microstructure characteristics of perovskite catalysts [36,37]. The selectivity of H_2 and CO_2 was high, and CO was kept low at 450 °C, indicating that the WGS reaction was the dominant reaction under low-temperature conditions. The 96.0% ethanol conversion with 71.3% hydrogen selectivity at 700 °C over the $LaNi_{0.9}Cu_{0.1}O_{3-\lambda}$ catalyst was impressive. High H_2 selectivity and ethanol dehydrogenation in the ESR process under low temperatures might be attributed, synergistically, to the Cu-Ni interaction. High CO_2/CO and H_2/CO ratios of $LaNi_{0.9}Cu_{0.1}O_{3-\lambda}$ (Figure 6h,i) indicate that the addition of copper facilitates the WGS reaction, which is due to the strong interaction between the Cu-Ni particles and the high distribution of active elements on the catalysts, also suppressing the sintering of the metal. Figure 7 presents the scheme of the ethanol steam reforming process by $LaNi_xCu_{1-x}O_{3-\lambda}$ catalysts.

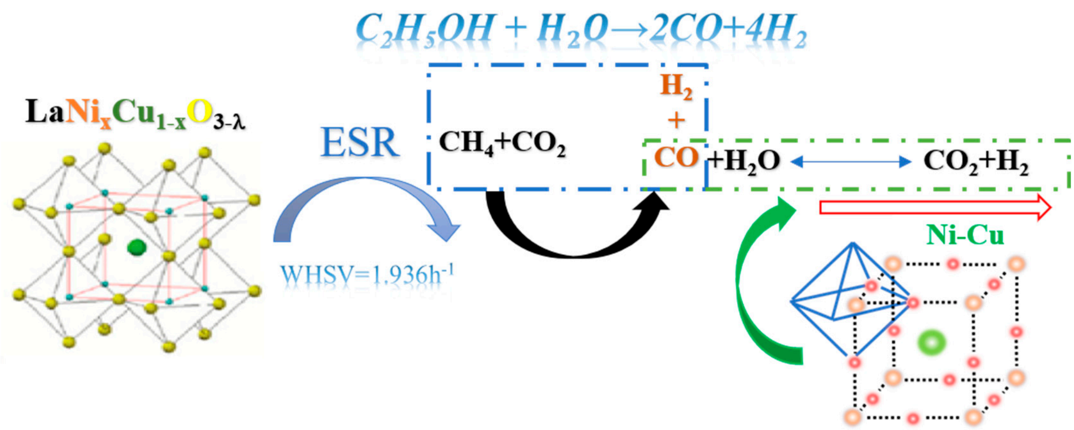

Figure 7. Scheme of ESR process by $LaNi_xCu_{1-x}O_{3-\lambda}$ catalysts.

The kinetic parameters of *E*a and k_0 between 450 and 700 °C, based on the conversions with temperatures, are shown in Table 2, and Arrhenius plots are shown in Figure 8. Linear relationships (R_0^2: 0.9936–0.9989) were calculated for three perovskite catalysts, which demonstrated that the power-law modeling with 1.0 order successfully described ethanol steam reforming and provided a good fit for the measurements of the rate constant at 450–700 °C. From the Arrhenius plot reported in Figure 8, the estimated values of energy of activation for ESR over the $LaNiO_{3-\lambda}$, $LaNi_{0.5}Cu_{0.5}O_{3-\lambda}$, and $LaNi_{0.9}Cu_{0.1}O_{3-\lambda}$ catalyst was calculated to be 83.6, 69.1, and 57.9 kJ/mol, respectively. As a comparison, the *E*a value of the $LaNi_{0.9}Cu_{0.1}O_{3-\lambda}$ was lower than those of $LaNiO_{3-\lambda}$ and $LaNi_{0.5}Cu_{0.5}O_{3-\lambda}$, showing that the catalytic activity was improved with Cu doping.

Table 2. Kinetics parameters of ESR by $LaNi_xCu_{1-x}O_{3-\lambda}$ catalysts.

Catalysts	*E*a (KJ·mol^{-1})	k_0 (s^{-1})	R_0^2
$LaNiO_{3-\lambda}$	83.6	1.6801	0.9948
$LaNi_{0.5}Cu_{0.5}O_{3-\lambda}$	69.1	1.7332	0.9936
$LaNi_{0.9}Cu_{0.1}O_{3-\lambda}$	57.9	0.9920	0.9989

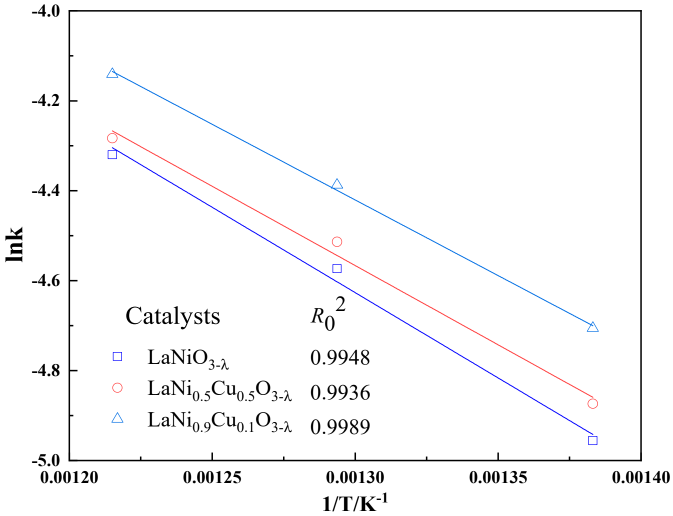

Figure 8. Arrhenius plot of ESR over the catalysts.

2.3. Stability Tests

The stability of the catalysts in ESR is one of the most essential challenges for hydrogen production. In studying the catalytic stability behavior of the $LaNi_xCu_{1-x}O_{3-\lambda}$ catalysts, a series of long-term experimental tests with $LaNi_xCu_{1-x}O_{3-\lambda}$ at 700 °C, S/C = 3, P = 1 atm, and WHSV = 1.936 h^{-1} were performed, and the results are shown in Figure 9. As can be seen, the catalyst with low copper content (x = 0.9) showed the best stability, and the conversion of ethanol and the H_2 selectivity of the $LaNi_{0.9}Cu_{0.1}O_{3-\lambda}$ catalyst remained at 95.3% and 71%, respectively, throughout the long reaction time, while the ethanol conversion and H_2 selectivity of the $LaNi_{0.5}Cu_{0.5}O_{3-\lambda}$ catalyst gradually decreased with the extension of the reaction time. Due to the proper addition of copper, copper and nickel interacted synergistically, inhibiting carbon deposition and enhancing the stability of the catalyst. However, the excessive addition of copper made facilitated the production of carbon deposition, reducing active component stability of the catalyst. Naturally, the steam reforming of ethanol was a complex system, which involved different ethanol conversion procedures and several secondary reactions between the by-products of the reforming process. Ethanol is not a thermally stable reactant and can be converted to other organic products before reaching, or through, homogeneous/heterogeneous reactions on the catalyst bed. Therefore, undesirable by-products are produced. These side reactions would occur together with steam reforming, thus reducing the hydrogen yield. It is worth noting that steam reforming is not the only reaction that can help hydrogen production. The steam reforming of acetone and methane also played an important role in product distribution, especially at high temperatures. During the stability test, the CH_4 selectivity of all the samples was very low, which showed that the methanation was inhibited due to its exothermic property under the reaction conditions.

After the stability tests, the used $LaNi_xCu_{1-x}O_{3-\lambda}$ catalysts were analyzed. The textural properties are shown in Table 3, and TGA-DTG is shown in Figure 10. As can be seen in Figure 10, first, as the temperature increases, there is a slight mass gain at 250–380 °C, which might be due to the re-oxidation of the Ni species [38]. With a further increase in temperature, the catalysts weight continuously decreases. Finally, the weight of the catalysts remains unchanged, indicating that the coke deposition had been completely removed. The weight gain in the oxidation process was considerably smaller in comparison to the weight loss from carbon combustion, which could be negligible [39]. It can be seen that the amount of coke deposition was arranged as follows: $LaNi_{0.9}Cu_{0.1}O_{3-\lambda}$ (3.66%), $LaNiO_{3-\lambda}$ (5.87%), and $LaNi_{0.5}Cu_{0.5}O_{3-\lambda}$ (19.78%); and the amount of coke deposition was consistent with the area of the TGA-DTG curve peaks. After the decoration of 0.1 copper, the peak of the DTG curve shifted to a lower temperature, which proved that coke depositions formed on catalysts were easier to oxidize and remove. The proper doping of copper created a strong interaction between copper and nickel, inhibiting the sintering of nickel, enhancing the stability of the catalyst, and reducing the rate of coke deposition, and the oxygen evolution and the synergistic effect between the elements may be important for this catalyst [40]. However, excessive Cu doping accelerated the formation of coke deposition and greatly affected the stability of ESR. Meanwhile, as can be seen in Table 3, the specific surface areas of the three catalysts slightly decreased, which might be due to the sintering of metals and carbon deposition. Moreover, a small amount of mass loss of active components occurred, which might be due to the heating and volatilizing of the metals on the catalysts.

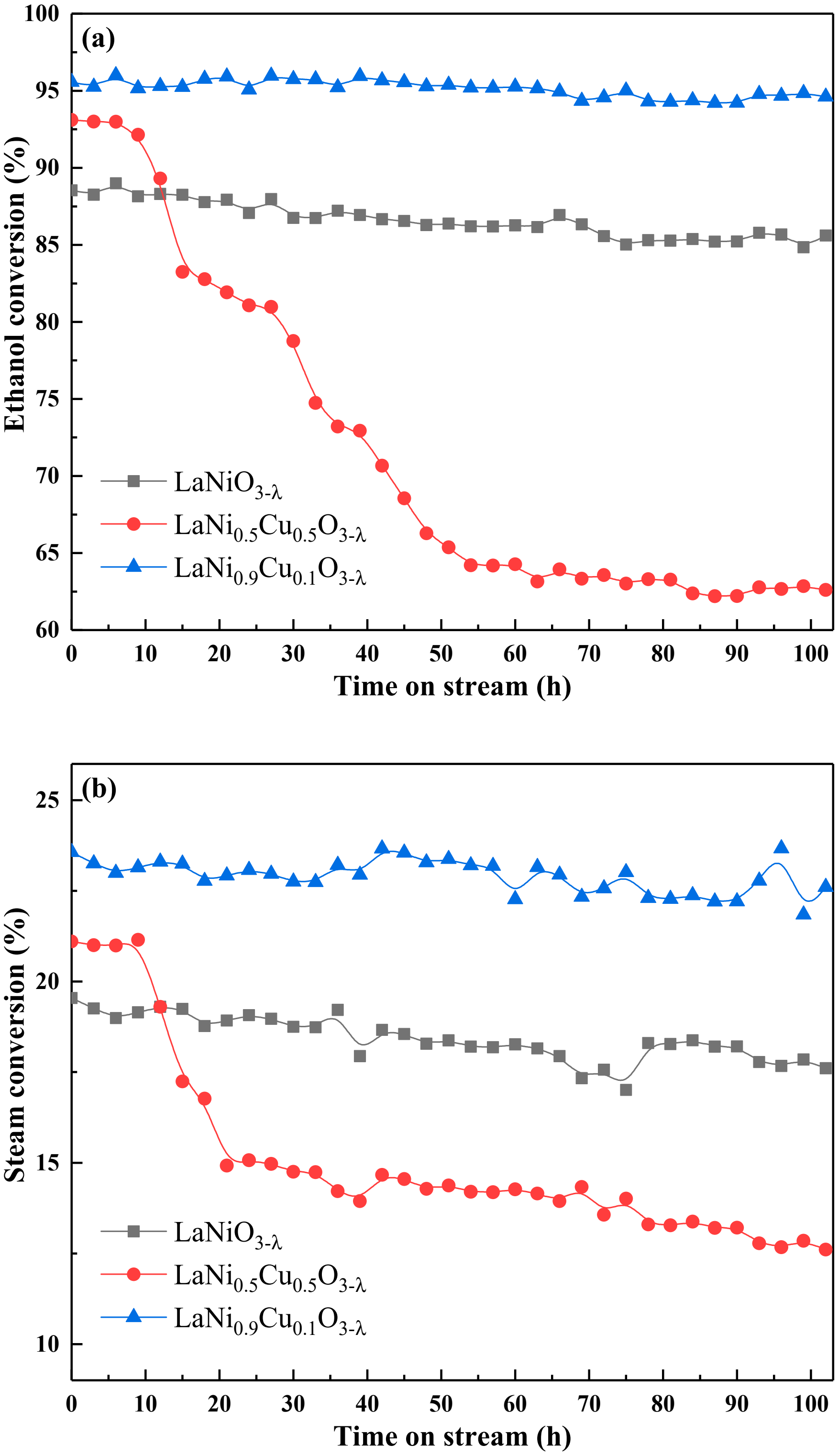

Figure 9. *Cont.*

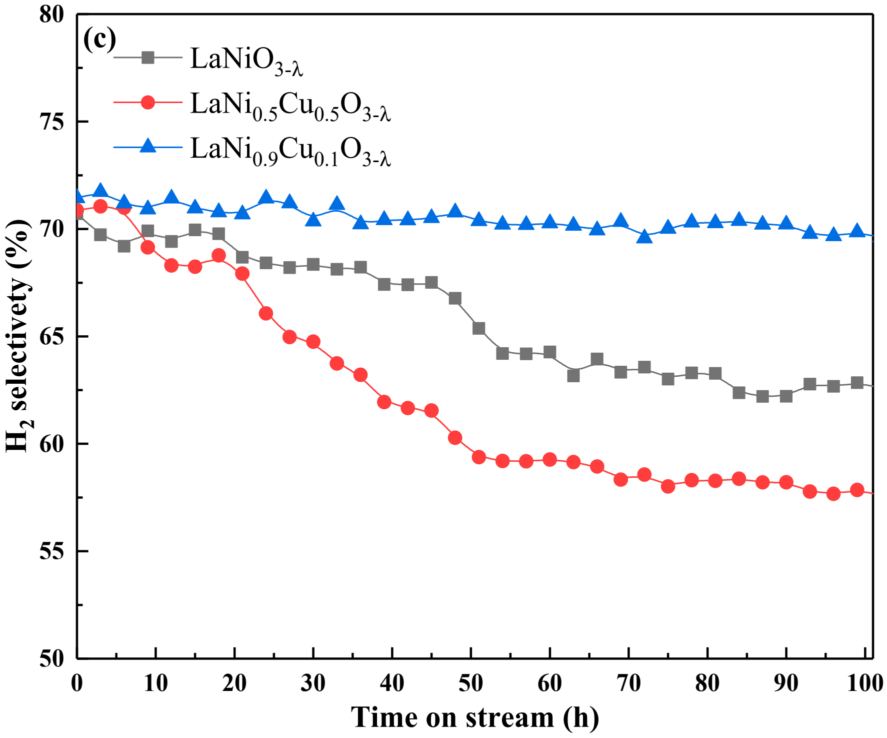

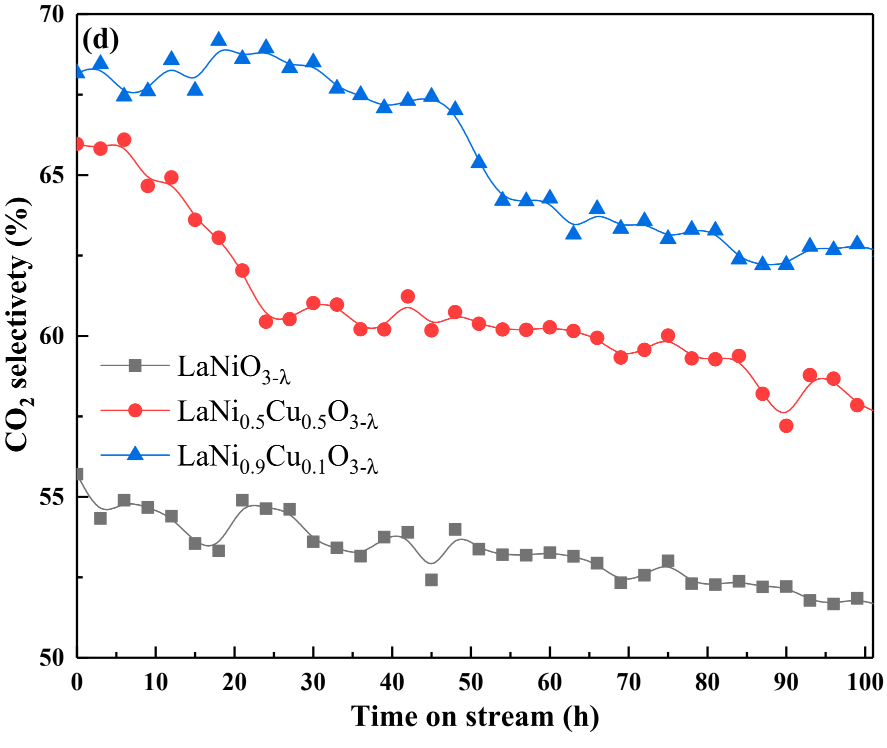

Figure 9. *Cont.*

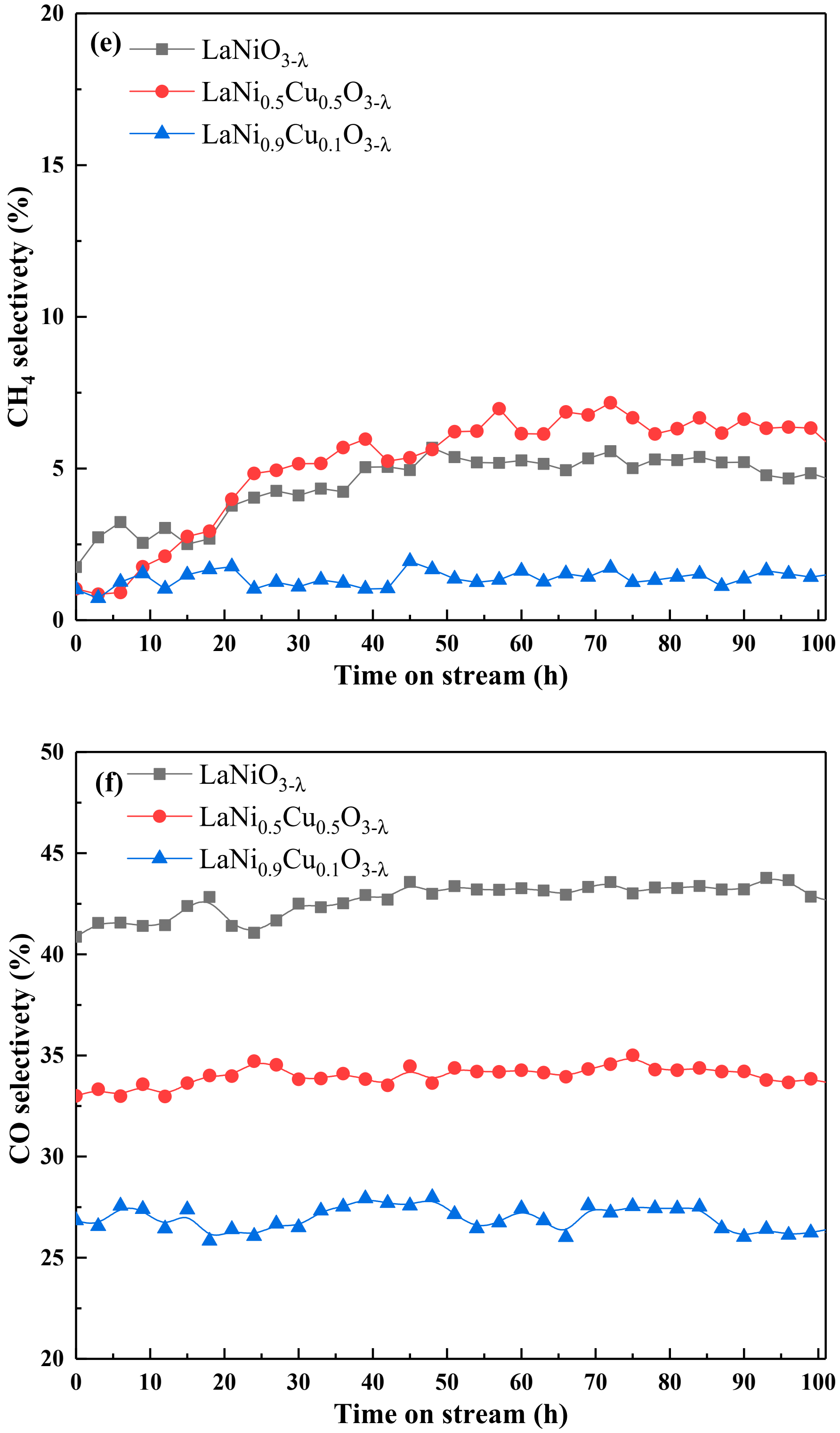

Figure 9. The conversion or selectivity for the long-term ESR testing of the catalysts: (**a**) ethanol; (**b**) steam; (**c**) H_2; (**d**) CO_2; (**e**) CH_4; (**f**) CO. The reaction conditions in ESR: T = 700 °C, P = 1 atm, WHSV = 1.936 h^{-1}, S/C is 3:1.

Table 3. The properties of the catalysts after 100 h test time on stream studies.

Catalysts	S_{BET} (m^2/g)	V_{pore} (cm^3/g)	Content (mmol/g)		Average Pore Size (nm)
			Ni	Cu	
$LaNiO_{3-\lambda}$	4.49	0.250	6.81	-	45.7
$LaNi_{0.5}Cu_{0.5}O_{3-\lambda}$	5.13	0.225	3.38	3.37	41.0
$LaNi_{0.9}Cu_{0.1}O_{3-\lambda}$	6.70	0.262	6.15	0.65	42.8

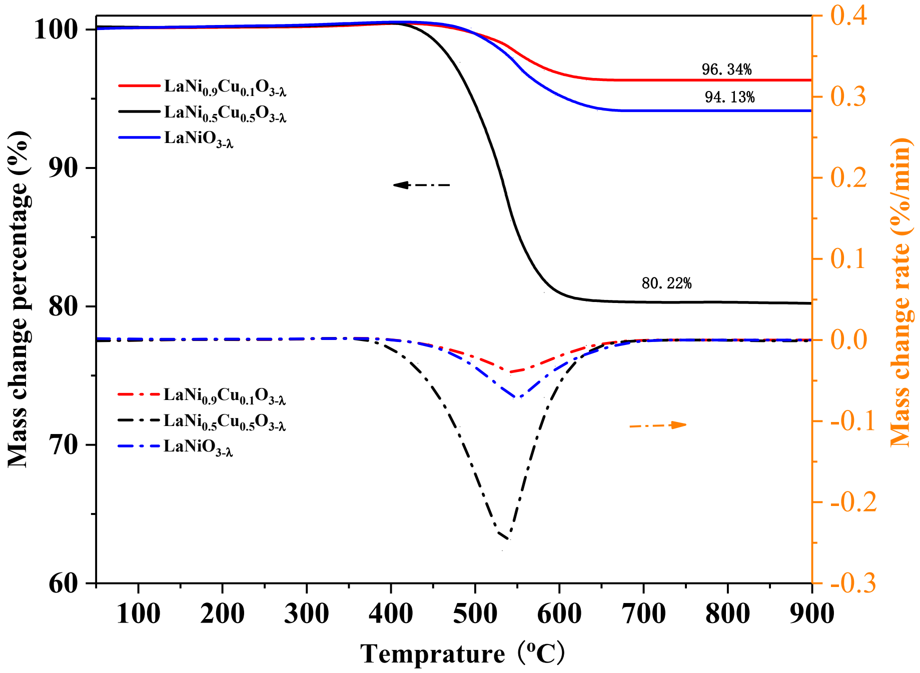

Figure 10. TGA and DTG curves of $LaNi_xCu_{1-x}O_{3-\lambda}$ catalysts after 100 h ESR reaction.

3. Experimental Section and Calculations

3.1. Preparation of $LaNi_xCu_{1-x}O_{3-\lambda}$ Catalyst

The $LaNi_xCu_{1-x}O_{3-\lambda}$ perovskite-type catalysts were prepared via the co-precipitation technique with structure agents [38]. The process of the preparation is shown schematically in Figure 11. First, $La(NO_3)_3{\cdot}6H_2O$ (99%), $Ni(NO_3)_2{\cdot}6H_2O$ (99%), and $Cu(NO_3)_2{\cdot}6H_2O$ (99%) were all dissolved in three different molar ratios of 1:1:0, 1:0.9:0.1, and 1:0.5:0.5 in a 100 mL aqueous solution of Na_2CO_3. Ethanol and ethylene glycol were added to the structure to induce porous formation. The pH value of the mixed solution was controlled by the NaOH solution, with the pH rising to 10 ± 0.5. The suspension was aged at room temperature for 15 h. After that, the resulted slurry was filtered and then rinsed repeatedly with deionized water until the filtrate was clear and transparent. It was then dried at 120 °C for 18 h in a drying oven and ultimately calcined at 450 °C for 2 h and then 850 °C for 6 h (heating rate of 5 °C/min) under air conditions. The same method was also used for the synthesis of an unpromoted Cu catalyst.

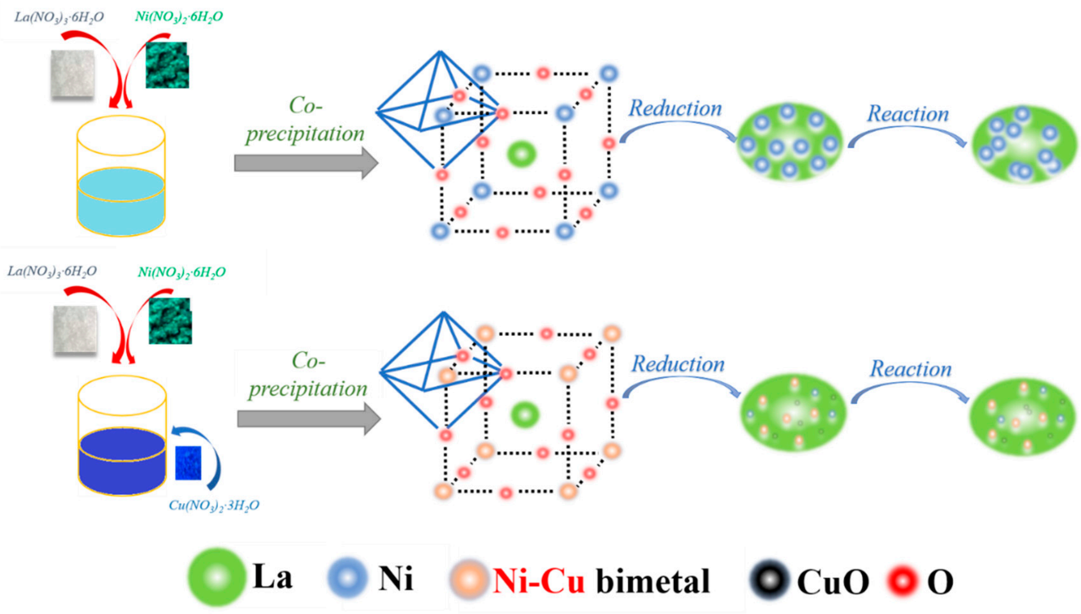

Figure 11. Synthesis of the $LaNi_xCu_{1-x}O_{3-\lambda}$ catalysts for ESR.

3.2. Characterization

N_2 adsorption–desorption experiments were used to test the specific surface area (S_{BET}) and pore diameter distribution with an F-Sorb 2400 device (Woodinville, WA, USA). First, the impurities on the catalyst's surface were removed at 150 °C for 5 h. XRD was performed to analyze the crystalline phases fractions of the catalysts and determine surface crystal size by a Siemens (Munich, Germany) D5000 instrument (Cu Ka radiation, 40 kV, 30 mA). Temperature-programmed H_2-TPR was used to identify the metal–support interaction of $LaNi_xCu_{1-x}O_{3-\lambda}$ using a Quantachrome (Boynton Beach, FL, USA) OBP-1 instrument with a temperature-programmed detector. SEM with EDS mapping was devoted to analyzing the surface morphology of the catalysts (LEO 1530). Before the SEM analysis, the samples were dispersed in ethanol by ultrasound, and drops of suspension were coated on the Cu-grid coated with carbon film and dried in air. TGA experiments were performed to analyze the $LaNi_xCu_{1-x}O_{3-\lambda}$ precursor and carbon deposition of spent catalysts with a thermogravimetric apparatus (TGA 2000, Canberra, Australia) under an airflow rate of 300 mL/min and at a heating rate of 15 °C/min.

3.3. Activity and Stability Test

The schematic diagram of the experimental two-stage fixed-bed reactor system is shown in Figure 12. About 1.0 g of catalyst was loaded in the center of the quartz tube (Φ12 × 600 mm) in the fixed-bed reactor. The feedstock used was an aqueous ethanol solution prepared by dissolving ethanol (99.7%) in deionized water. Before the experiments, the catalysts were first reduced at 650 °C for 3h with a 300 mL/h flow of about 5 vol.% H_2 and 95 vol.% N_2. For a typical experiment, the water and ethanol were mixed and injected into a preheater located at the top of the reactor (the first stage reactor) with a steam–carbon (S/C) ratio of 3, and it was first heated and vaporized. The mixture vapor of ethanol and steam was then passed through the catalyst layer in the second-stage reactor, where it reacts and readily produces H_2. During all experiments, the weight hourly space velocity (WHSV) was controlled at 1.936 h^{-1}. The outlet product gases, including H_2, CO, CH_4, and CO_2, were detected and analyzed using chromatography (GC7890).

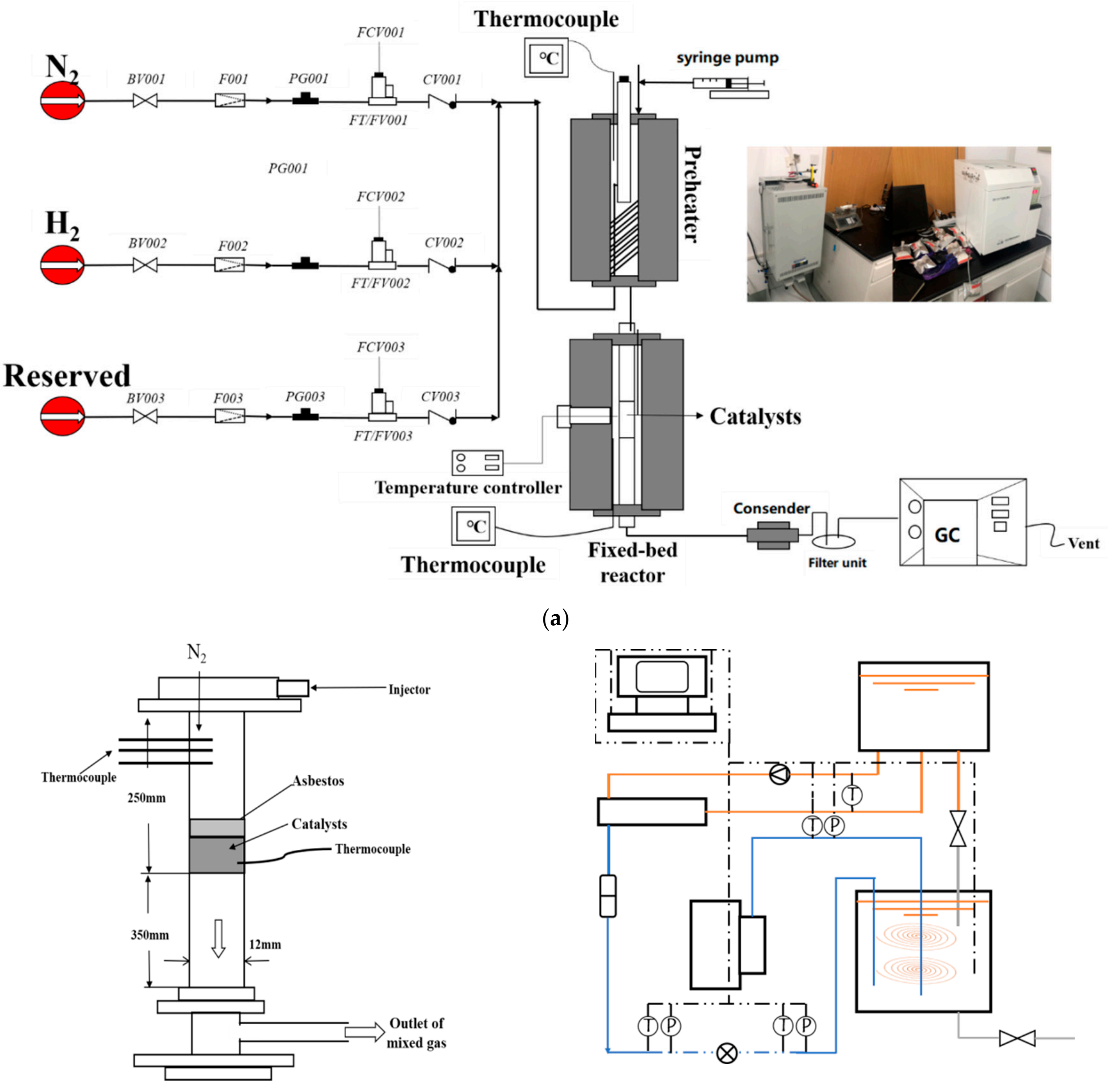

(**a**)

(**b**) (**c**)

Figure 12. Schematic diagram of the experimental equipment (**a**), the fixed-bed reactor (**b**), and the liquid mixture preheater (**c**).

3.4. Data Analysis and Calculation

The activity of the catalysts was evaluated by calculating the ethanol conversion (X_{et}), the steam conversion (X_{H2O}), and the selectivity of H_2, CO, CH_4, and CO_2 (*Sel*, *i*). The formulae are as follows:

$$X_{\mathrm{et}}(\%) = \frac{F_{Et,in} - F_{Et,out}}{F_{Et,in}} \times 100 \tag{1}$$

$$X_{H_2O}(\%) = \frac{F_{H_2O,in} - F_{H_2O,out}}{F_{H_2O,in}} \times 100 = \frac{F_{dry,out} - 3X_{et}F_{Et,in}}{F_{H_2O,in}} \tag{2}$$

$$\mathrm{Sel}.H_2(\%) = \frac{1}{6} \times \frac{\dot{F}_{H_2,out}}{X_{\mathrm{et}} \times F_{ethanol,in}} \times 100 \tag{3}$$

$$\mathrm{Sel}.i(\%) = \frac{(\%i) \times j}{\sum (\%i) \times j} \times 100 \tag{4}$$

$$F_{dry,out} = \frac{F_{N_2,in}}{1 - (Sel_{H_2} + Sel_{CH_4} + Sel_{CO_2} + Sel_{CO})} \times 100 \tag{5}$$

where *F* represents the molar rate (mol/min); and *j* is the number of carbon atoms in a species with the carbon atom.

3.5. Determination of the Equilibrium Constant for the Ethanol Steam Reforming (ESR) Reaction

To compare experimental data and evaluate the activity of perovskite-type catalysts, a non-stoichiometric thermodynamic method based on the chemical equilibrium was used to calculate the conversion rate of reactants and gas products [41,42]. In this approach, an accurate estimation of the system on an initial thermodynamic equilibrium is not needed. The minimization of Gibbs free energy (G) was used:

$$dG = \sum_{i=1}^{N} \mu_i dn_i = 0 \tag{6}$$

where μ_i is the component i's chemical potential, and n_i is its concentration, as follows:

$$\sum_{i=1}^{N} a_{ji} n_i = b_j, j = 1, \ldots, M \tag{7}$$

where a_{ji} is the number of j type atoms in i species; and b_j refers to the number of j type atoms. In this system, Equation (8) can be obtained:

$$\Delta G_i^f / RT + ln(n_i/n_T) + lnP + ln\hat{\varphi}_i + \sum_{j=1}^{M} \lambda_j a_{ji}/RT = 0, i = 1, \ldots, N \tag{8}$$

where $\hat{\varphi}$ is the fugacity coefficient in the gases mixture calculated via the Redlich–Kwong equation; and ΔG_i^f is the standard Gibbs free energy of formation from the thermodynamic handbooks. n_T is defined as follows:

$$n_T = \sum_{i=1}^{N} n_i, i = 1, \ldots, N \tag{9}$$

Thermodynamic equilibrium calculations, including the N + M + 1 non-linear equation in the constrained conditions of ESR, were solved, and the mole fractions of the conversion and products in an equilibrium system were obtained at various temperatures [30]. The effects of temperature on the thermodynamic constants (K) were calculated via the following equations:

$$ln\left(\frac{K_1}{K_2}\right) = \frac{-\Delta H^0}{R}\left(\frac{1}{T_1} - \frac{1}{T_2}\right) \tag{10}$$

$$lnK = \frac{-\Delta G^0}{RT} \tag{11}$$

3.6. Reaction Kinetics

The fixed-bed reactor assumes that the reacting gases are ideally mixed in the radial direction, and their flows and velocities through the fixed-bed are understood as constant patterns over time. Axial diffusion does not take place [42].

Some of the criteria for ESR in a fixed-bed reactor were tested and evaluated to ensure that the data collected are in the true kinetic regime and that transport effects are not significant, including the following:

$$L/d_p > 50 \text{ and } Pe > Pe, \text{min.} \tag{12}$$

In this study, $L/d_p > 80$; $Pe > 50$. The power-law type of general equation was used to test the kinetics of ethanol steam reforming:

$$-r_A = kc_{ethanol}^{n} c_{H_2O}^{m} \tag{13}$$

The relationship between conversion and rate can be given as follows:

$$-r_A dw = F_0 dx_{ethanol} \tag{14}$$

where dw represents the mass of the catalyst, = l and $-r_A$ is the disappearance of ethanol in moles per unit of catalyst mass per of unit time. The rate constant of ethanol steam reforming using the first-order reaction was calculated via an integral plug flow reactor model:

$$k = \frac{F_0}{c_0 w} ln \frac{1}{1 - x_{ethanol}} \tag{15}$$

where c_0 is the inlet concentration of ethanol in the carrier gas. The Arrhenius-type expression describing the reaction rate constant is

$$k = k_0 exp(-\frac{Ea}{RT}) \tag{16}$$

where Ea is the apparent activation energy, kJ/mol; and k_0 is the pre-exponential factor, s^{-1}. Ea and k_0 in Equation (16) were regressed based on the Arrhenius equation with k values calculated at a set of different T.

4. Conclusions

In this study, a series of $LaNi_xCu_{1-x}O_{3-\lambda}$ (x = 0.5, 0.9, 1.0) catalysts were synthesized via a co-precipitation method and tested for ESR at 450–700 °C. SEM and mapping images of the fresh catalyst showed that $LaNi_{0.9}Cu_{0.1}O_{3-\lambda}$ has the best homogenization and distribution of elements. Compared with the $LaNiO_{3-\lambda}$ catalyst, the enhanced activity of the $LaNi_{0.9}Cu_{0.1}O_{3-\lambda}$ catalyst for the ESR reaction was verified by the high conversion of ethanol (96.0%) and H_2 selectivity (71.3%) at 700 °C. Furthermore, the addition of copper can help to reduce the reaction temperature as well; the CO_2/CO and H_2/CO of $LaNi_{0.9}Cu_{0.1}O_{3-\lambda}$ indicated that the addition of copper facilitates the WGS reaction, which is due to the strong interaction between the copper and nickel particles and the high distribution of active elements of Cu and Ni on the $LaNi_xCu_{1-x}O_{3-\lambda}$ catalysts. Meanwhile, the $LaNi_{0.9}Cu_{0.1}O_{3-\lambda}$ catalyst showed the preferable resistance to carbon formation and deposition, as well as high activity and good stability.

Author Contributions: C.R.: Data curation, Investigation, Writing—review & editing. B.D.: Conceptualization, Writing—review & editing, Investigation. N.C.: Investigation. H.Z.: Investigation. All authors have read and agreed to the published version of the manuscript.

Funding: This research received no external funding.

Data Availability Statement: Data are contained within the article.

Acknowledgments: This work was supported by the Natural Science Foundation of China [grant numbers 52476211 and 51876130] and supported by Capacity Building Plan for some Non-military Universities and Colleges of Shanghai Scientific Committee (No. 18060502600).

Conflicts of Interest: The authors declare that they have no known competing financial interests or personal relationships that could have appeared to influence the work reported in this paper.

References

1. Dou, B.; Wu, K.; Zhang, H.; Chen, B.; Chen, H.; Xu, Y. Sorption-enhanced chemical looping steam reforming of glycerol with CO_2 in-situ capture and utilization. *Chem. Eng. J.* **2023**, *452*, 139703. [CrossRef]
2. Chen, B.; Rickard, S.; Bao, Z.; Wu, Z.; Kidder, M.K.; Savara, A. Evidence of redox cycling as a sub-mechanism in hydrogen production during ethanol steam reforming over $La_{0.7}Sr_{0.3}MnO_{3-x}$ perovskite oxide catalysts. *Appl. Surf. Sci.* **2023**, *617*, 156603. [CrossRef]
3. Kourtelesis, M.; Panagiotopoulou, P.; Verykios, X.E. Influence of structural parameters on the reaction of low temperature ethanol steam reforming over Pt/Al_2O_3 catalysts. *Catal. Today* **2015**, *258*, 247–255. [CrossRef]

4. Dou, B.; Wang, K.; Jiang, B.; Song, Y.; Zhang, C.; Chen, H.; Xu, Y. Fluidized-bed gasification combined continuous sorption-enhanced steam reforming system to continuous hydrogen production from waste plastic. *Int. J. Hydrogen Energy* **2016**, *41*, 3803–3810. [CrossRef]
5. de la Piscina, P.R.; Homs, N. Use of biofuels to produce hydrogen (reformation processes). *Chem. Soc. Rev.* **2008**, *37*, 2459–2467. [CrossRef] [PubMed]
6. Mondal, T.; Pant, K.K.; Dalai, A.K. Oxidative and non-oxidative steam reforming of crude bio-ethanol for hydrogen production over Rh promoted Ni/CeO_2-ZrO_2 catalyst. *Appl. Catal. A Gen.* **2015**, *499*, 19–31. [CrossRef]
7. Vaidya, P.D.; Rodrigues, A.E. Insight into steam reforming of ethanol to produce hydrogen for fuel cells. *Chem. Eng. J.* **2006**, *117*, 39–49. [CrossRef]
8. da Silva, A.G.; Robles-Dutenhefner, P.A.; Dias, A.; Fajardo, H.V.; Lovón, A.S.; Lovón-Quintana, J.J.; Valença, G.P. Gold, palladium and gold–palladium supported on silica catalysts prepared by sol–gel method: Synthesis, characterization and catalytic behavior in the ethanol steam reforming. *J. Sol-Gel Sci. Technol.* **2013**, *67*, 273–281. [CrossRef]
9. Ghita, D.; Stanica Ezeanu, D.; Cursaru, D.; Rosca, P. Hydrogen production by steam reforming of bioethanol over Pt based catalysts. *Rev. Chim.* **2016**, *67*, 145–149.
10. Bilal, M.; Jackson, S.D. Ethanol steam reforming over Pt/Al_2O_3 and Rh/Al_2O_3 catalysts: The effect of impurities on selectivity and catalyst deactivation. *Appl. Catal. A Gen.* **2017**, *529*, 98–107. [CrossRef]
11. Mudiyanselage, K.; Al-Shankiti, I.; Foulis, A.; Llorca, J.; Idriss, H. Reactions of ethanol over CeO_2 and Ru/CeO_2 catalysts. *Appl. Catal. B Environ.* **2016**, *197*, 198–205. [CrossRef]
12. Lindstrm, B.; Pettersson, L.J. Hydrogen generation by steam reforming of methanol over copper-based catalysts for fuel cell applications. *Int. J. Hydrogen Energy* **2001**, *26*, 923–933. [CrossRef]
13. Lua, A.C.; Wang, H.Y. Hydrogen production by catalytic decomposition of methane over Ni-Cu-Co alloy particles. *Appl. Catal. B Environ.* **2014**, *156–157*, 84–93. [CrossRef]
14. Dou, B.; Zhang, H.; Cui, G.; Cui, G.; Wang, Z.; Jiang, B.; Wang, K.; Chen, H.; Xu, Y. Hydrogen production and reduction of Ni-based oxygen carriers during chemical looping steam reforming of ethanol in a fixed-bed reactor. *Int. J. Hydrogen Energy* **2017**, *26*, 217–230. [CrossRef]
15. Dou, B.; Song, Y.; Wang, C.; Wang, C.; Chen, H.; Xu, Y. Hydrogen production from catalytic steam reforming of biodiesel byproduct glycerol: Issues and challenges. *Renew. Sustain. Energy Rev.* **2014**, *30*, 950–960. [CrossRef]
16. Hu, M.; Laghari, M.; Cui, B.; Xiao, B.; Zhang, B.; Guo, D. Catalytic cracking of biomass tar over char supported nickel catalyst. *Energy* **2018**, *145*, 228–237. [CrossRef]
17. De Lima, S.M.; Pena, M.A.; Fierro, J.L.; Assaf, J.M. $La_{1-x}Ca_xNiO_3$ Perovskite Oxides: Characterization and Catalytic Reactivity in Dry Reforming of Methane. *Catal. Lett.* **2008**, *124*, 195–203. [CrossRef]
18. Nalbandian, L.; Evdou, A.; Zaspalis, V. $La_{1-x}Sr_xM_yFe_{1-y}O_{3-\delta}$ perovskites as oxygen-carrier materials for chemical-looping reforming. *Int. J. Hydrogen Energy* **2011**, *36*, 6657–6670. [CrossRef]
19. de Lima, S.M.; da Silva, A.M.; da Costa, L.O.; Assaf, J.M.; Mattos, L.V.; Sarkari, R.; Venugopal, A.; Noronha, F.B. Hydrogen production through oxidative steam reforming of ethanol over Ni-based catalysts derived from $La_{1-x}Ce_xNiO_3$ perovskite-type oxides. *Appl. Catal. B Environ.* **2012**, *121–122*, 1–9. [CrossRef]
20. Morales, M.; Segarra, M. Steam reforming and oxidative steam reforming of ethanol over $La_{0.6}Sr_{0.4}CoO_{3-\delta}$ perovskite as catalyst precursor for hydrogen production. *Appl. Catal. A Gen.* **2015**, *502*, 305–311. [CrossRef]
21. Agüero, F.N.; Morales, M.R.; Larrégola, S.; Izurieta, E.M.; Lopez, E.; Cadús, L.E. $La_{1-x}Ca_xAl_{1-y}Ni_yO_3$ perovskites used as precursors of nickel based catalysts for ethanol steam reforming. *Int. J. Hydrogen Energy* **2015**, *40*, 15510–15520. [CrossRef]
22. Urasaki, K.; Tokunaga, K.; Sekine, Y.; Matsukata, M.; Kikuchi, E. Production of hydrogen by steam reforming of ethanol over cobalt and nickel catalysts supported on perovskite-type oxides. *Catal. Commun.* **2008**, *9*, 600–604. [CrossRef]
23. Wang, L.; Li, D.; Koike, M.; Koso, S.; Nakagawa, Y.; Xu, Y.; Tomishige, K. Catalytic performance and characterization of Ni-Fe catalysts for the steam reforming of tar from biomass pyrolysis to synthesis gas. *Appl. Catal. A Gen.* **2011**, *392*, 248–255. [CrossRef]
24. Heo, D.H.; Lee, R.; Hwang, J.H.; Sohn, J.M. The effect of addition of Ca, K and Mn over Ni-based catalyst on steam reforming of toluene as model tar compound. *Catal. Today* **2016**, *265*, 95–102. [CrossRef]
25. Nejat, T.; Jalalinezhad, P.; Hormozi, F.; Bahrami, Z. Hydrogen production from steam reforming of ethanol over Ni-Co bimetallic catalysts and MCM-41 as support. *J. Taiwan Inst. Chem. Eng.* **2019**, *97*, 216–226. [CrossRef]
26. Ávila-Neto, C.N.; Oliveira, K.D.; Oliveira, K.F.; Arouca, A.M.; Ferreira, R.A.; Hori, C.E. Interconnection between feed composition and Ni/Co ratio in (La-Ni-Co-O) based perovskites and its effects on the stability of LPG steam reforming. *Appl. Catal. A Gen.* **2017**, *550*, 184–197. [CrossRef]
27. Yu, X.P.; Chu, W.; Wang, N.; Ma, F. Hydrogen Production by Ethanol Steam Reforming on NiCuMgAl Catalysts Derived from Hydrotalcite-Like Precursors. *Catal. Lett.* **2011**, *141*, 1228–1236. [CrossRef]
28. Liu, J.Y.; Su, W.N.; Rick, J.; Yang, S.C.; Cheng, J.H.; Pan, C.J.; Lee, J.F.; Hwang, B.J. Hierarchical Copper-Decorated Nickel Nanocatalysts Supported on La_2O_3 for Low-Temperature Steam Reforming of Ethanol. *ChemSusChem* **2013**, *2*, 570–576. [CrossRef]

29. Lin, K.H.; Wang, C.B.; Chien, S.H. Catalytic performance of steam reforming of ethanol at low temperature over $LaNiO_3$ perovskite. *Int. J. Hydrogen Energy* **2013**, *38*, 3226–3232. [CrossRef]
30. Jing, Z.; Li, H.; Jiang, Z. The chemical interaction of support and active phase in sintering resistant $La_{0.8}Ca_{0.2}FeO_3$ perovskite catalysts. *Fuel* **2019**, *243*, 322–331. [CrossRef]
31. Gallego, G.S.; Mondragón, F.; Tatibouët, J.-M.; Barrault, J.; Batiot-Dupeyrat, C. Carbon dioxide reforming of methane over La_2NiO_4 as catalyst precursor-characterization of carbon deposition. *Catal. Today* **2008**, *133*, 200–209. [CrossRef]
32. Gallego, G.S.; Mondragón, F.; Barrault, J.; Tatibouët, J.-M.; Batiot-Dupeyrat, C. CO_2 reforming of CH_4 over La-Ni based perovskite precursors. *Appl. Catal. A Gen.* **2006**, *311*, 164–171. [CrossRef]
33. Barros, B.S.; Melo, D.M.; Libs, S.; Kiennemann, A. CO_2 reforming of methane over $La_2NiO_4/\alpha\text{-}Al_2O_3$ prepared by microwaveassisted self-combustion method. *Appl. Catal. A Gen.* **2010**, *378*, 69–75. [CrossRef]
34. Rynkowski, J.; Samulkiewicz, P.; Ladavos, A.; Pomonis, P. Catalytic performance of reduced $La_{2-x}Sr_xNiO_4$ perovskite-like oxides for CO_2 reforming of CH_4. *Appl. Catal. A Gen.* **2004**, *263*, 1–9. [CrossRef]
35. Li, Y.; Fu, Q.; Flytzani-Stephanopoulos, M. Low-temperature water-gas shift reaction over Cu- and Ni-loaded cerium oxide catalysts. *Appl. Catal. B Environ.* **2000**, *27*, 179–191. [CrossRef]
36. Sanchez, E.; Comelli, R. Hydrogen by glycerol steam reforming on a nickel-alumina catalyst: Deactivation processes and regeneration. *Int. J. Hydrogen Energy* **2012**, *37*, 14740–14746. [CrossRef]
37. Shen, Q.; Shao, Z.; Li, S.; Yang, G.; Sunden, B. Effects of B-site Al doping on microstructure characteristics and hydrogen production performance of novel $LaNixAl_{1-x}O_{3-\delta}$ perovskite in methanol steam reforming. *Energy* **2023**, *268*, 126540. [CrossRef]
38. Zhang, Q.; Li, L.; Jiang, B.; Wang, K.; Tang, D.; Dou, B. An intelligent oxygen carrier of $La_{2-x}Sr_xNiO_{4-\lambda}$ for hydrogen production by chemical looping reforming of ethanol. *Int. J. Hydrogen Energy* **2017**, *42*, 17102–17111. [CrossRef]
39. Zhang, Q.; Li, L.; Jiang, B.; Tang, D.; Dou, B. Hydrogen by chemical looping reforming of ethanol: The effect of promoters on $La_{2-x}M_xNiO_{4-\lambda}$ (M = Ca, Sr and Ce) oxygen carriers. *Chem. Eng. Sci.* **2017**, *174*, 259–267. [CrossRef]
40. Qiu, H.; Yuan, B.; Zhao, C.; Dang, J.; Zhang, C.; Wang, Q.; Xia, L.; Miao, H.; Yuan, J. A high-entropy and low-cobalt perovskite of $La_{0.7}Sr_{0.3}Co_{0.2}Mn_{0.2}Ni_{0.2}Fe_{0.2}Al_{0.2}O_{3-x}$ for both oxygen evolution and methanol oxidation reactions. *Int. J. Hydrogen Energy* **2024**, *51*, 593–604. [CrossRef]
41. Dou, B.; Zhang, H.; Cui, G.; Wang, Z.; Jiang, B.; Wang, K.; Chen, H.; Xu, Y. Hydrogen production by sorption-enhanced chemical looping steam reforming of ethanol in an alternating fixed-bed reactor: Sorbent to catalyst ratio dependencies. *Energy Convers. Manag.* **2018**, *1551*, 243–252. [CrossRef]
42. Wang, C.; Dou, B.; Chen, H.; Song, Y.; Xu, Y.; Du, X.; Luo, T.; Tan, C. Hydrogen Production from Steam Reforming of Glycerol by Ni-Mg-Al based Catalysts in a Fixed-bed Reactor. *Chem. Eng. J.* **2013**, *220*, 133–142. [CrossRef]